

# Initial, effective, and kinetic freeze-out temperatures from transverse momentum spectra in high energy proton(deuteron)-nucleus and nucleus-nucleus collisions

Muhammad Waqas, Fu-Hu Liu\*

*Institute of Theoretical Physics and State Key Laboratory of Quantum Optics and Quantum Optics Devices,  
Shanxi University, Taiyuan, Shanxi 030006, China*

**Abstract:** The transverse momentum spectra of charged particles produced in proton(deuteron)-nucleus and nucleus-nucleus collisions at high energies are analyzed by the Hagedorn thermal model and the standard distribution in terms of multi-component. The experimental data measured in central and peripheral gold-gold (Au-Au) and deuteron-gold ( $d$ -Au) collisions by the PHENIX Collaboration at the Relativistic Heavy Ion Collider (RHIC), as well as in central and peripheral lead-lead (Pb-Pb) and proton-lead ( $p$ -Pb) collisions by the ALICE Collaboration at the Large Hadron Collider (LHC) are fitted by the two models. The initial, effective, and kinetic freeze-out temperatures are then extracted from the fitting to the transverse momentum spectra. It is shown that the initial temperature is larger than the effective temperature, and the effective temperature is larger than the kinetic freeze-out temperature. The three types of temperatures in central collisions are comparable with those in peripheral collisions, and those at the LHC are comparable with those at the RHIC.

**Keywords:** Transverse momentum spectra, initial temperature, kinetic freeze-out temperature, nucleus-nucleus collisions

**PACS:** 14.40.-n, 14.20.-c, 24.10.Pa

## 1 Introduction

The concept of temperature used in thermodynamics and statistical mechanics [1] is also used in subatomic physics due to similar thermal and statistical property. At least the initial, chemical freeze-out, thermal or kinetic freeze-out, and effective temperatures are used in high energy collisions. The initial temperature describes the excitation degree of interacting system at the initial stage of collisions. The chemical freeze-out temperature describes the excitation degree of interacting system at the stage of chemical freeze-out, where the ratios of different types of particles are no longer changed. The kinetic freeze-out temperature describes the excitation degree of interacting system at the stage of kinetic freeze-out, where the transverse momentum spectra are no longer changed. The effective temperature describes the sum of the excitation degree of interacting system and the effect of transverse flow at the stage of kinetic freeze-out, where the transverse flow resulted from the impact and squeeze reflects the hydrodynamic expansion of interacting systems.

The initial temperature has less studies in the community due to undefined method, though it should be based on the particle spectra. The chemical freeze-out temperature can be obtained from the particle ratios [2, 3, 4, 5]. The kinetic freeze-out temperature can be obtained from the transverse momentum spectra, in the case of getting rid of the transverse flow effect and leaving only the contribution of random thermal motion [6, 7, 8, 9, 10]. If the temperature extracted from the transverse momentum spectra also contains the contribution of transverse flow, this type of temperature is not the kinetic freeze-out temperature, but the effective temperature called by us. The initial, chemical freeze-out, and kinetic freeze-out temperatures are “real” temperatures. The effective temperature is not a “real” temperature.

Generally, the initial stage of collisions happens earlier than the stages of chemical and kinetic freeze-outs. The initial temperature should be the largest among the three “real” temperatures. The initial stage of collisions is also possible to be simultaneous with the stage of chemical freeze-out. This also results possibly

\*E-mail: fuhuliu@163.com; fuhuliu@sxu.edu.cn

in the initial temperature to be equal to the chemical freeze-out temperature. Similarly, the stage of chemical freeze-out is simultaneous with or earlier than that of kinetic freeze-out. This results in the chemical freeze-out temperature to be equal to or larger than the kinetic freeze-out temperature. Because of two contributions, the effective temperature is often larger than the kinetic freeze-out temperature. In most cases, one has the initial temperature, chemical freeze-out temperature, effective temperature, and kinetic freeze-out temperature to reduce in turn.

Due to the definiteness of particle ratios at given condition such as at mid-rapidity in central collisions at given collision energy, the chemical freeze-out temperature can be measured correspondingly by the thermal and statistical model [2, 3, 4, 5]. Comparatively, the initial, effective, and kinetic freeze-out temperatures are model dependent due to the fact that different functions or distributions are used to fit the transverse momentum spectra [6, 7, 8, 9, 10]. At the same time, the limiting value of chemical freeze-out temperature at very high energy is knowable, and the limiting values of initial, effective, and kinetic freeze-out temperatures if available at high energy are difficult to predict due to their erratic trends.

It is unquestioned that the mentioned temperatures are related to study the phase diagram in the temperature related spaces, such as the temperatures as functions of transverse flow velocity, baryon chemical potential, collision centrality, system size, particle rapidity, and collision energy. To study systematically these temperature related functions are a huge project, in particular for the dependences of temperatures on collision energy. As a beginning of the project, the dependences of temperatures on collision centrality can be studied. Naturally, the studies of dependences of temperatures on these quantities are useful for us to understand the mechanisms of multi-particle production and system evolution. Although the initial (kinetic freeze-out) temperature is model dependent in most cases, we hope to use a model independent method to obtain it. The effective temperature is definitely model dependent, we shall not pay much attention to it.

It should be noted that there are different methods [11] to extract the kinetic freeze-out temperature from the transverse momentum spectra in high energy collisions [10]. These methods include, but are not limited to, the blast-wave model with the Boltzmann statistics [6, 7, 8], the blast-wave model with the Tsallis statistics [9, 12, 13], an alternative method [7, 14, 15, 16, 17]

which describes the transverse momentum spectra by using a Boltzmann distribution [18] and the intercept in the effective temperature versus particle mass is regarded as the kinetic freeze-out temperature, and the same alternative method but using a Tsallis distribution [18, 19]. Our recent work [11] shows that the four methods are harmonious in the dependences of kinetic freeze-out temperature on collision centrality and energy, though the absolute values are different in some cases.

In this paper, the transverse momentum spectra of positively and negatively charged pions ( $\pi^+$  and  $\pi^-$ ), positively and negatively charged kaons ( $K^+$  and  $K^-$ ), and protons ( $p$ ) and antiprotons ( $\bar{p}$ ) produced in central and peripheral gold-gold (Au-Au) and deuteron-gold ( $d$ -Au) collisions at the Relativistic Heavy Ion Collider (RHIC) [20, 21], as well as in central and peripheral lead-lead (Pb-Pb) and proton-lead ( $p$ -Pb) collisions at the Large Hadron Collider (LHC) [22, 23, 24] are fitted by the Hagedorn thermal model [25] and Boltzmann distribution [18] in terms of multi-component which is harmonious with a multisource thermal model used in our previous work [10]. The related temperatures which include the initial, effective, and kinetic freeze-out temperatures are then extracted from the fittings. In particular, the alternative method is used to extract the kinetic freeze-out temperature.

The remainder of this paper is structured as follows. The formalism and method are shortly described in Section 2. Results and discussion are given in Section 3. In Section 4, we summarize our main observations and conclusions.

## 2 Formalism and method

There are two main processes of multi-particle productions in high energy collisions, namely the soft excitation and hard scattering processes. For the two main processes, one can use different formalisms to describe the transverse momentum spectra of charged particles. Generally, in the descriptions, the soft excitation process has many choices of formalisms, and the hard scattering process has very limited choices of formalisms.

For the soft excitation process, the choices include, but are not limited to, the Hagedorn thermal model (the statistical-bootstrap model) [25], the (multi-)standard distribution [18], the Tsallis and related distributions with various formalisms [19], the blast-wave model with Boltzmann statistics [6, 7, 8], the blast-wave model with

Tsallis statistics [9], etc. To focus our attention on the effective temperature and then the initial and kinetic freeze-out temperatures according to the transverse momentum spectra, we use only the Hagedorn thermal model [25] and the standard distribution [18] in terms of multi-component as examples in the present work. The chemical freeze-out temperature needs systematically the particle ratios, which is beyond the focus of our attention and is not discussed in the present work.

According to ref. [25], the Hagedorn thermal model results in the transverse momentum ( $p_T$ ) distribution, in terms of the probability density function, at the mid-rapidity (the rapidity of the center-of-mass of interacting system in the center-of-mass system) to be

$$f_1(p_T) = \frac{1}{N} \frac{dN}{dp_T} = C_1 p_T \sqrt{p_T^2 + m_0^2} \times \sum_{n=1}^{\infty} (-S)^{n+1} K_1 \left( n \frac{\sqrt{p_T^2 + m_0^2}}{T_1} \right), \quad (1)$$

where  $N$ ,  $C_1$ ,  $m_0$ ,  $n$ ,  $K_1$ , and  $T_1$  denote the particle number, normalization constant, particle rest mass, item number in the summation, modified Bessel function of the second kind, and effective temperature, respectively, and  $S = +1$  and  $-1$  for fermions and bosons respectively. Generally, to obtain suitable  $p_T$  distributions,  $n$  is taken to be 1–10 for pions, 1–5 for kaons, and 1 for nucleons and hyperons [25]. In Eq. (1), the chemical potential is not considered due to very small value and effect at RHIC and LHC energies.

For particles distributed in a wide rapidity ( $y$ ) range from the minimum rapidity  $y_{\min}$  to the maximum rapidity  $y_{\max}$ , and the mid-rapidity is in  $[y_{\min}, y_{\max}]$ , we have the  $p_T$  distribution to be

$$f_1(p_T) = C_1 p_T \sqrt{p_T^2 + m_0^2} \int_{y_{\min}}^{y_{\max}} \cosh y \times \sum_{n=1}^{\infty} (-S)^{n+1} K_1 \left( n \frac{\sqrt{p_T^2 + m_0^2} \cosh y}{T_1} \right) dy, \quad (2)$$

where the normalization constant  $C_1$  in Eq. (2) may be different from that in Eq. (1). Comparing with Eq. (1) which is the particular case of Eq. (2) with  $y = 0$ , Eq. (2) is more suitable to the particles distributed in a wide rapidity range. In some cases, the mid-rapidity is not in  $[y_{\min}, y_{\max}]$ . Then, we may transform the rapidity range by adding or subtracting a rapidity shift to cover the mid-rapidity, so that we can exclude the contribution of directional movement of the emission source.

In some cases, the Hagedorn thermal model is not enough to describe the spectra in low  $p_T$  region contributed by the soft process. A two-, three-, or even multi-component Hagedorn thermal model is needed. We have the multi-component model to be

$$f_1(p_T) = \sum_{i=1}^l k_{1i} C_{1i} p_T \sqrt{p_T^2 + m_0^2} \times \sum_{n=1}^{\infty} (-S)^{n+1} K_1 \left( n \frac{\sqrt{p_T^2 + m_0^2}}{T_{1i}} \right), \quad (3)$$

or

$$f_1(p_T) = \sum_{i=1}^l k_{1i} C_{1i} p_T \sqrt{p_T^2 + m_0^2} \int_{y_{\min}}^{y_{\max}} \cosh y \times \sum_{n=1}^{\infty} (-S)^{n+1} K_1 \left( n \frac{\sqrt{p_T^2 + m_0^2} \cosh y}{T_{1i}} \right) dy, \quad (4)$$

where  $l$  denotes the number of components, and  $k_{1i}$ ,  $C_{1i}$ , and  $T_{1i}$  denote the contribution fraction, normalization constant, and effective temperature corresponding to the  $i$ -th component respectively. In particular, the normalization results in  $\sum_{i=1}^l k_{1i} = 1$ , and the effective temperature averaged by weighting different components is  $T_1 = \sum_{i=1}^l k_{1i} T_{1i}$ . Generally,  $l \leq 3$ .

The standard distribution is a joint name of the Boltzmann, Fermi-Dirac, and Bose-Einstein distributions which base on the Boltzmann, Fermi-Dirac, and Bose-Einstein statistics, respectively, which correspond to  $S = 0$ ,  $+1$ , and  $-1$ , respectively [18]. At the mid-rapidity or in the rapidity range  $[y_{\min}, y_{\max}]$  which covers the mid-rapidity, the standard distribution is

$$f_2(p_T) = C_2 p_T \sqrt{p_T^2 + m_0^2} \times \left[ \exp \left( \frac{\sqrt{p_T^2 + m_0^2}}{T_2} \right) + S \right]^{-1} \quad (5)$$

or

$$f_2(p_T) = C_2 p_T \sqrt{p_T^2 + m_0^2} \int_{y_{\min}}^{y_{\max}} \cosh y \times \left[ \exp \left( \frac{\sqrt{p_T^2 + m_0^2} \cosh y}{T_2} \right) + S \right]^{-1} dy, \quad (6)$$

where  $C_2$  and  $T_2$  are the normalization constant and effective temperature respectively. If the rapidity range  $[y_{\min}, y_{\max}]$  does not cover the mid-rapidity, we need to shift it to cover the mid-rapidity.

In some cases, the standard distribution is not enough to describe the spectra in low  $p_T$  region contributed by the soft process. A two-, three-, or even

multi-component standard distribution is needed. We have the multi-component standard distribution to be

$$f_2(p_T) = \sum_{i=1}^l k_{2i} C_{2i} p_T \sqrt{p_T^2 + m_0^2} \times \left[ \exp \left( \frac{\sqrt{p_T^2 + m_0^2}}{T_{2i}} \right) + S \right]^{-1}, \quad (7)$$

or

$$f_2(p_T) = \sum_{i=1}^l k_{2i} C_{2i} p_T \sqrt{p_T^2 + m_0^2} \int_{y_{\min}}^{y_{\max}} \cosh y \times \left[ \exp \left( \frac{\sqrt{p_T^2 + m_0^2} \cosh y}{T_{2i}} \right) + S \right]^{-1} dy, \quad (8)$$

where  $k_{2i}$ ,  $C_{2i}$ , and  $T_{2i}$  denote the contribution fraction, normalization constant, and effective temperature corresponding to the  $i$ -th component respectively. In particular, the normalization results in  $\sum_{i=1}^l k_{2i} = 1$ , and the effective temperature averaged by weighting different components is  $T_2 = \sum_{i=1}^l k_{2i} T_{2i}$ .

It should be noted that the rapidity  $y$  used in Eqs. (4) and (8) are for particles, but not for fireballs. If we study rapidity spectra, we should use these fireballs at different rapidities  $y_x$ . In the case of studying  $p_T$  spectra,  $y_x$  should be directly shifted to 0 so that the kinetic energy of directional movement of fireballs can be removed from temperature which is contributed by thermal motion, but not directional movement, of particles.

For a not too wide  $p_T$  spectrum, the above equations such as Eqs. (3) or (4) and (7) or (8) can be used to describe the  $p_T$  spectrum and to extract the effective temperature. For a wide  $p_T$  spectrum, we have to consider the contribution of hard scattering process. In some cases, although the  $p_T$  spectrum is wide, the contribution of hard scattering process in high- $p_T$  regions is negligible. We can only concern the contribution of soft excitation process in low- $p_T$  region. If the spectrum of high- $p_T$  region is non-negligible, we can use an inverse power-law, i.e. the Hagedorn function [25]

$$f_H(p_T) = A p_T \left( 1 + \frac{p_T}{p_0} \right)^{-n} \quad (9)$$

to describe the contribution of hard scattering process, where  $p_0$  and  $n$  are free parameters, and  $A$  is the normalization constant related to the free parameters. The inverse power-law is obtained from the quantum chromodynamics (QCD) calculus [26, 27, 28] and has three

revisions [29, 30, 31, 32, 33, 34, 35] which will not be discussed further in the present work.

In the case of considering both the contributions of soft excitation and hard scattering processes, the experimental  $p_T$  spectrum distributed in a wide range can be described by a superposition, i.e.

$$f_0(p_T) = k_0 f_S(p_T) + (1 - k_0) f_H(p_T), \quad (10)$$

where  $k_0$  denotes the contribution fraction of the soft excitation process and  $f_S(p_T)$  denotes one of Eqs. (3) or (4) and (7) or (8). According to Hagedorn's model [25], we may also use the usual step function

$$f_0(p_T) = A_1 \theta(p_1 - p_T) f_S(p_T) + A_2 \theta(p_T - p_1) f_H(p_T), \quad (11)$$

to superpose the two functions, where  $A_1$  and  $A_2$  are constants which result in the two components to be equal to each other at  $p_T = p_1 \approx 2 \sim 3$  GeV/ $c$ .

Eqs. (10) and (11) are two different superpositions. In Eq. (10), the soft component contributes from 0 up to  $2 \sim 3$  GeV/ $c$  or a little more, and the hard component contributes in the whole  $p_T$  range. The main contributor in the low- $p_T$  range is the soft component and the only contributor in the high- $p_T$  range is the hard component. In Eq. (11), the soft component contributes from 0 up to  $p_1$ , and the hard component contributes from  $p_1$  up to the maximum. There is no mixed range for the two components, though the curve is possibly not smooth at their boundary  $p_1$ . We shall use only the first component in Eq. (11) due to not too wide  $p_T$  range studied in the present work. In particular,  $f_S(p_T)$  is exactly Eqs. (4) and (8) respectively, in which  $l = 1, 2$ , or 3 for different sets of data.

### 3 Results and discussion

Figure 1 presents the transverse momentum spectra,  $(1/2\pi p_T) d^2 N / dp_T dy$ , of (a)-(c)  $\pi^+$ ,  $K^+$ , and  $p$ , as well as (b)-(d)  $\pi^-$ ,  $K^-$ , and  $\bar{p}$  produced in (a)-(b) 0–5% and (c)-(d) 60–92% Au-Au collisions at center-of-mass energy per nucleon pair  $\sqrt{s_{NN}} = 200$  GeV. The squares, circles, and triangles represent respectively the experimental data of  $\pi^+$  ( $\pi^-$ ),  $K^+$  ( $K^-$ ), and  $p$  ( $\bar{p}$ ) measured by the PHENIX Collaboration in the pseudorapidity range  $|\eta| < 0.35$  [20]. The solid and dotted curves are our results fitted by the first component in Eq. (11) through Eqs. (4) and (8) respectively, where we have coded the equation ourselves by Matlab which has intrinsic functions to perform calculations for Bessel

and modified Bessel functions. The values of related parameters are listed in Tables 1 and 2 with the value of  $\chi^2$  and the number of degree of freedom (dof) in terms of  $\chi^2/\text{dof}$ . The ratios of data/fit corresponding to panels (a)–(d) are presented by panels (a\*)–(d\*) respectively, where the closed squares, circles, and triangles are the results for  $\pi^+$  ( $\pi^-$ ),  $K^+$  ( $K^-$ ), and  $p$  ( $\bar{p}$ ) due to Eqs. (4), and the open squares, circles, and triangles are the results for  $\pi^+$  ( $\pi^-$ ),  $K^+$  ( $K^-$ ), and  $p$  ( $\bar{p}$ ) due to Eqs. (8). One can see that the two models fit well the trends of the experimental data in low- $p_T$  region in Au-Au collisions at the top RHIC energy.

Figure 2 is the same as Fig. 1, but it shows the spectra in (a)–(b) 0–20% and (c)–(d) 60–88%  $d$ -Au collisions at  $\sqrt{s_{NN}} = 200$  GeV. The symbols represent the experimental data measured by the PHENIX Collaboration in  $|\eta| < 0.35$  [21]. The curves are our fitted results and the related parameters are listed in Tables 1 and 2 with  $\chi^2/\text{dof}$ . One can see that the two models fit well the trends of the experimental data in low- $p_T$  region in  $d$ -Au collisions at the top RHIC energy.

The transverse momentum spectra of (a)–(b)  $\pi^+ + \pi^-$ ,  $K^+ + K^-$ , and  $p + \bar{p}$  produced in (a) 0–5% and (b) 70–80% Pb-Pb collisions at  $\sqrt{s_{NN}} = 2.76$  TeV are displayed in Fig. 3. For the clarity, the spectra for  $\pi^+ + \pi^-$  and  $K^+ + K^-$  are multiplied by 100 and 10 respectively, which are shown in the panels. The squares, circles, and triangles represent respectively the experimental data of  $\pi^+ + \pi^-$ ,  $K^+ + K^-$ , and  $p + \bar{p}$  measured by the ALICE Collaboration in the rapidity range  $|y| < 0.5$  [22, 23]. The solid and dotted curves are our results fitted by the first component in Eq. (11) through Eqs. (4) and (8) respectively. The related parameters are listed in Tables 1 and 2 with  $\chi^2/\text{dof}$ . The ratios of data/fit corresponding to panels (a) and (b) are presented by panels (a\*) and (b\*) respectively, where the closed and open symbols are the results due to Eqs. (4) and (8) respectively. One can see that the two models fit well the trends of the experimental data in low- $p_T$  region in Pb-Pb collisions at the LHC energy.

Figure 4 is the same as Fig. 3, but it shows the spectra in (a)–(b) 0–5% and (c)–(d) 60–88%  $p$ -Pb collisions at  $\sqrt{s_{NN}} = 5.02$  TeV. The symbols represent the experimental data measured by the ALICE Collaboration in  $0 < y < 0.5$  [24]. The curves are our fitted results and the related parameters are listed in Tables 1 and 2 with  $\chi^2/\text{dof}$ . One can see that the two models fit well the trends of the experimental data in low- $p_T$  region in  $d$ -Au collisions at the top RHIC energy.

As effective temperatures,  $T_1$  and  $T_2$  depend on  $m_0$ ,

which are shown in Figs. 5(a) and 5(b) respectively. Different symbols shown in the panel represent the results from positive or negative particles produced in central or peripheral Au-Au or  $d$ -Au collisions, or from positive plus negative particles produced in central or peripheral Pb-Pb or  $p$ -Pb collisions. These symbols represent the results weighted different contribution fractions in two or three-component listed in Tables 1 and 2. The dashed lines are the fitting results by linear functions for negative particles in Au-Au or  $d$ -Au collisions, and the solid lines are for other cases. The intercepts and slopes of these linear functions are listed in Table 3 with  $\chi^2$ , where  $\text{dof} = 1$  is neglected. Similar to Figs. 5(a) and 5(b), the dependences of  $T_1$  and  $T_2$  on centrality  $C$  are displayed in Figs. 5(c) and 5(d) respectively. The different symbols represent different  $T_1$  ( $T_2$ ) for different cases shown in the panels, and  $T_1$  ( $T_2$ ) obtained from the spectra of positive and negative particles are not distinguished to avoid trivialness. One can see that the effective temperature obtained from the spectrum of particles with large mass is obviously larger than that with small mass. The effective temperature in central collisions is slightly larger than or equal to that in peripheral collisions. The effective temperature at LHC energy is comparable with that at RHIC energy. Meanwhile, the effective temperature in Au-Au (Pb-Pb) collisions is comparable with that in  $d$ -Au ( $p$ -Pb) collisions.

We can regard the intercepts in the linear relation between the effective temperature and particle mass in Fig. 5(a) and 5(b) as the kinetic freeze-out temperatures  $T_{01}$  and  $T_{02}$  [10, 20] respectively. Figures 6(a) and 6(b) show the dependences of  $T_{01}$  and  $T_{02}$  on  $C$  respectively, where the symbols represent the intercepts obtained from Figs. 5(a) and 5(b) and listed in Table 3. One can see that the kinetic freeze-out temperature in central collisions is slightly larger than or equal to that in peripheral collisions. The kinetic freeze-out temperatures in collisions at LHC and RHIC energies are comparable with each other. Meanwhile, the kinetic freeze-out temperatures in Au-Au (Pb-Pb) and  $d$ -Au ( $p$ -Pb) collisions are comparable with each other. These results confirm our previous works [36, 11], though the absolute values are different due to different methods. These results are also in agreement with the effective temperature in general trends in different centralities, at different energies, and in different collision systems.

Figures 7(a) and 7 (b) show the dependences of mean  $p_T$  ( $\langle p_T \rangle_1$  and  $\langle p_T \rangle_2$ ) on  $m_0$  obtained from the fits of multi-component Hagedorn thermal model and standard distribution respectively. Figures 7(c) and 7 (d)

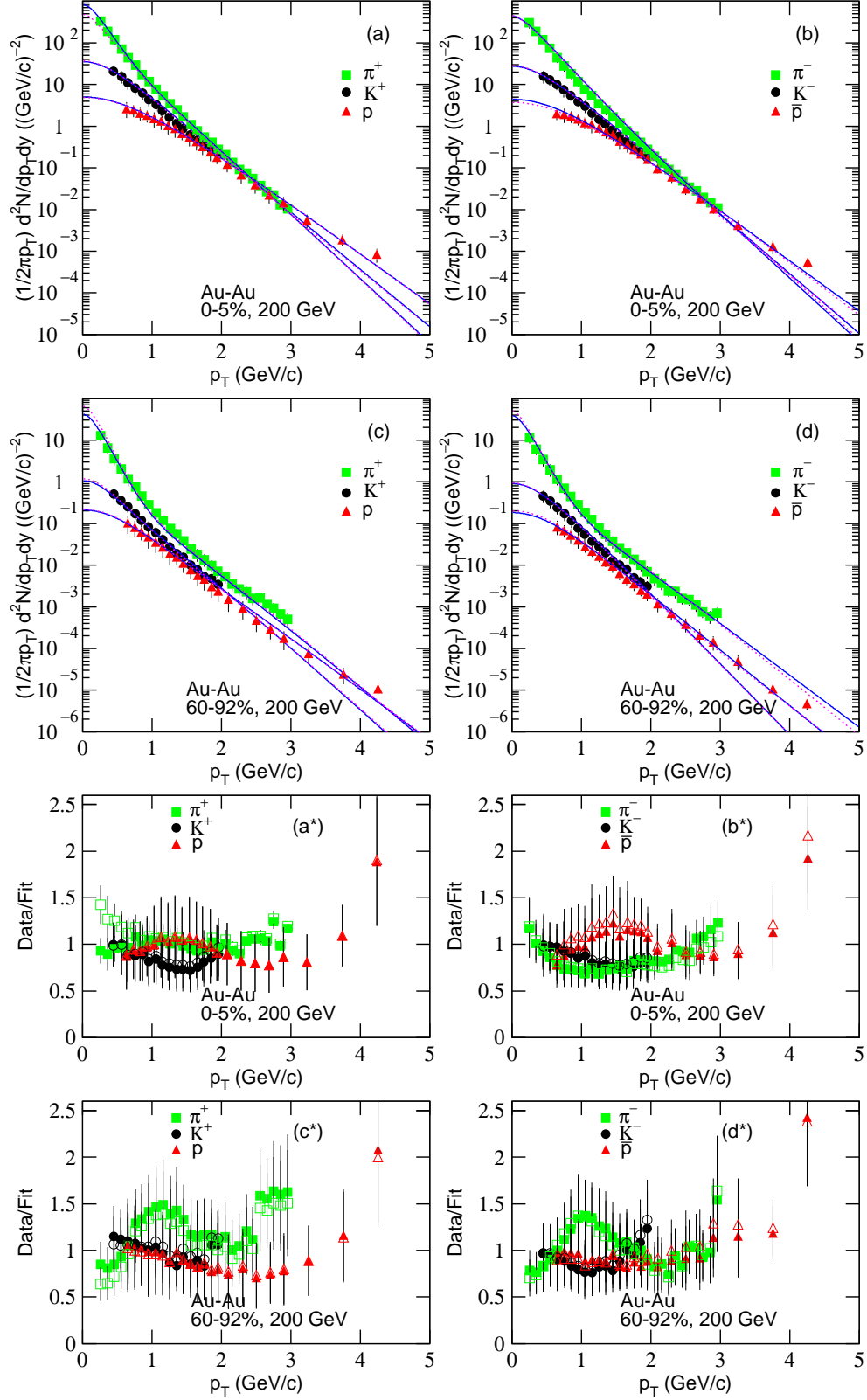


Fig. 1. Transverse momentum spectra of (a)-(c)  $\pi^+$ ,  $K^+$ , and  $p$ , as well as (b)-(d)  $\pi^-$ ,  $K^-$ , and  $\bar{p}$  produced in (a)-(b) 0-5% and (c)-(d) 60-92% Au-Au collisions at  $\sqrt{s_{NN}} = 200$  GeV. The symbols represent the experimental data measured by the PHENIX Collaboration in  $|\eta| < 0.35$  [20]. The solid and dotted curves are our results fitted by Eqs. (4) and (8) respectively. The ratios of data/fit corresponding to panels (a)-(d) are presented by panels (a\*)-(d\*) respectively, where the closed and open symbols are the results due to Eqs. (4) and (8) respectively.

Table 1. Values of free parameters ( $T_{11}$ ,  $T_{12}$ ,  $T_{13}$  if available,  $k_{11}$ , and  $k_{12}$  if available), normalization constant ( $N_0$ ), and  $\chi^2/\text{dof}$  corresponding to the solid curves in Figs. 1–4.

Figure	Centrality	Particle	$T_{11}$ (GeV)	$T_{12}$ (GeV)	$T_{13}$ (GeV)	$k_{11}$	$k_{12}$	$N_0$	$\chi^2/\text{dof}$
Fig. 1 Au-Au 200 GeV	0–5%	$\pi^+$	$0.267 \pm 0.009$	$0.544 \pm 0.006$	—	$0.70 \pm 0.05$	—	$50.95 \pm 4.00$	315/25
		$K^+$	$0.460 \pm 0.006$	$0.605 \pm 0.007$	$0.614 \pm 0.005$	$0.46 \pm 0.08$	$0.20 \pm 0.04$	$8.70 \pm 0.70$	9/13
		$p$	$0.685 \pm 0.005$	$0.686 \pm 0.005$	—	$0.55 \pm 0.02$	—	$2.51 \pm 0.20$	5/19
		$\pi^-$	$0.378 \pm 0.006$	$0.551 \pm 0.008$	—	$0.70 \pm 0.05$	—	$44.95 \pm 5.00$	39/25
		$K^-$	$0.437 \pm 0.008$	$0.584 \pm 0.008$	—	$0.16 \pm 0.06$	—	$7.20 \pm 0.60$	10/13
		$\bar{p}$	$0.647 \pm 0.005$	$0.773 \pm 0.006$	—	$0.92 \pm 0.16$	—	$2.12 \pm 0.14$	7/19
	60–92%	$\pi^+$	$0.238 \pm 0.008$	$0.636 \pm 0.006$	$0.715 \pm 0.007$	$0.90 \pm 0.05$	$0.11 \pm 0.01$	$1.83 \pm 0.18$	17/25
		$K^+$	$0.260 \pm 0.006$	$0.560 \pm 0.008$	—	$0.35 \pm 0.09$	—	$0.17 \pm 0.02$	2/13
		$p$	$0.395 \pm 0.005$	$0.666 \pm 0.006$	—	$0.48 \pm 0.04$	—	$0.070 \pm 0.005$	6/19
		$\pi^-$	$0.235 \pm 0.005$	$0.323 \pm 0.008$	$0.669 \pm 0.007$	$0.80 \pm 0.07$	$0.10 \pm 0.01$	$1.74 \pm 0.16$	11/25
		$K^-$	$0.375 \pm 0.008$	$0.490 \pm 0.005$	—	$0.24 \pm 0.08$	—	$0.18 \pm 0.02$	5/13
		$\bar{p}$	$0.418 \pm 0.014$	$0.624 \pm 0.005$	—	$0.58 \pm 0.04$	—	$0.060 \pm 0.010$	6/19
Fig. 2 d-Au 200 GeV	0–20%	$\pi^+$	$0.316 \pm 0.007$	$0.515 \pm 0.005$	$0.978 \pm 0.008$	$0.60 \pm 0.05$	$0.36 \pm 0.04$	$0.99 \pm 0.05$	6/21
		$K^+$	$0.348 \pm 0.008$	$0.478 \pm 0.008$	$0.864 \pm 0.005$	$0.42 \pm 0.03$	$0.29 \pm 0.03$	$0.13 \pm 0.01$	1/18
		$p$	$0.625 \pm 0.005$	$0.752 \pm 0.004$	—	$0.56 \pm 0.08$	—	$0.055 \pm 0.004$	9/21
		$\pi^-$	$0.290 \pm 0.008$	$0.506 \pm 0.006$	$1.100 \pm 0.002$	$0.51 \pm 0.03$	$0.46 \pm 0.04$	$0.99 \pm 0.06$	5/21
		$K^-$	$0.378 \pm 0.007$	$0.393 \pm 0.012$	$0.852 \pm 0.008$	$0.40 \pm 0.03$	$0.30 \pm 0.03$	$0.13 \pm 0.01$	2/18
		$\bar{p}$	$0.490 \pm 0.008$	$0.612 \pm 0.007$	$0.712 \pm 0.008$	$0.20 \pm 0.06$	$0.45 \pm 0.07$	$0.050 \pm 0.004$	15/21
	60–88%	$\pi^+$	$0.296 \pm 0.008$	$0.666 \pm 0.003$	$0.670 \pm 0.005$	$0.74 \pm 0.04$	$0.74 \pm 0.10$	$0.21 \pm 0.02$	23/21
		$K^+$	$0.307 \pm 0.008$	$0.324 \pm 0.014$	$0.778 \pm 0.006$	$0.42 \pm 0.02$	$0.30 \pm 0.03$	$0.036 \pm 0.003$	2/18
		$p$	$0.410 \pm 0.009$	$0.788 \pm 0.006$	—	$0.75 \pm 0.02$	—	$0.015 \pm 0.001$	12/21
		$\pi^-$	$0.258 \pm 0.008$	$0.650 \pm 0.007$	$0.765 \pm 0.004$	$0.70 \pm 0.01$	$0.30 \pm 0.01$	$0.21 \pm 0.02$	21/21
		$K^-$	$0.318 \pm 0.010$	$0.450 \pm 0.011$	$0.885 \pm 0.005$	$0.38 \pm 0.03$	$0.32 \pm 0.02$	$0.035 \pm 0.002$	4/18
		$\bar{p}$	$0.160 \pm 0.010$	$0.280 \pm 0.010$	$0.600 \pm 0.005$	$0.08 \pm 0.01$	$0.05 \pm 0.01$	$0.011 \pm 0.001$	19/21
Fig. 3 Pb-Pb 2.76 TeV	0–5%	$\pi^+ + \pi^-$	$0.236 \pm 0.012$	$0.597 \pm 0.005$	—	$0.41 \pm 0.04$	—	$240.00 \pm 15.00$	28/38
		$K^+ + K^-$	$0.674 \pm 0.008$	$0.684 \pm 0.009$	—	$0.30 \pm 0.05$	—	$36.00 \pm 1.70$	30/33
		$p + \bar{p}$	$0.970 \pm 0.009$	$1.050 \pm 0.001$	$1.150 \pm 0.001$	$0.65 \pm 0.05$	$0.84 \pm 0.06$	$9.70 \pm 0.33$	9/34
	70–80%	$\pi^+ + \pi^-$	$0.272 \pm 0.013$	$0.683 \pm 0.006$	—	$0.74 \pm 0.02$	—	$5.60 \pm 0.29$	458/38
		$K^+ + K^-$	$0.183 \pm 0.013$	$0.620 \pm 0.005$	—	$0.16 \pm 0.04$	—	$0.81 \pm 0.04$	14/33
		$p + \bar{p}$	$0.393 \pm 0.016$	$0.401 \pm 0.012$	$0.730 \pm 0.006$	$0.01 \pm 0.01$	$0.02 \pm 0.01$	$0.30 \pm 0.01$	9/34
Fig. 4 p-Pb 5.02 TeV	0–5%	$\pi^+ + \pi^-$	$0.215 \pm 0.014$	$0.600 \pm 0.003$	$0.729 \pm 0.007$	$0.54 \pm 0.04$	$0.09 \pm 0.03$	$6.73 \pm 0.33$	20/38
		$K^+ + K^-$	$0.260 \pm 0.014$	$0.294 \pm 0.014$	$0.796 \pm 0.006$	$0.10 \pm 0.02$	$0.12 \pm 0.04$	$0.95 \pm 0.04$	5/28
		$p + \bar{p}$	$0.878 \pm 0.010$	$0.930 \pm 0.009$	—	$0.56 \pm 0.16$	—	$0.37 \pm 0.02$	19/36
	60–80%	$\pi^+ + \pi^-$	$0.203 \pm 0.013$	$0.365 \pm 0.009$	$0.750 \pm 0.006$	$0.49 \pm 0.02$	$0.29 \pm 0.02$	$1.65 \pm 0.10$	41/38
		$K^+ + K^-$	$0.219 \pm 0.008$	$0.327 \pm 0.009$	$0.693 \pm 0.005$	$0.21 \pm 0.04$	$0.13 \pm 0.01$	$0.19 \pm 0.01$	14/28
		$p + \bar{p}$	$0.434 \pm 0.016$	$0.860 \pm 0.011$	$0.971 \pm 0.007$	$0.54 \pm 0.03$	$0.15 \pm 0.05$	$0.19 \pm 0.01$	17/36

Table 2. Values of free parameters ( $T_{21}$ ,  $T_{22}$ ,  $T_{23}$  if available,  $k_{21}$ , and  $k_{22}$  if available), normalization constant ( $N_0$ ), and  $\chi^2/\text{dof}$  corresponding to the dashed curves in Figs. 1–4.

Figure	Centrality	Particle	$T_{21}$ (GeV)	$T_{22}$ (GeV)	$T_{23}$ (GeV)	$k_{21}$	$k_{22}$	$N_0$	$\chi^2/\text{dof}$
Fig. 1 Au-Au 200 GeV	0–5%	$\pi^+$	$0.148 \pm 0.008$	$0.261 \pm 0.004$	—	$0.08 \pm 0.01$	—	$50.95 \pm 5.00$	404/25
		$K^+$	$0.225 \pm 0.007$	$0.299 \pm 0.005$	—	$0.13 \pm 0.06$	—	$8.73 \pm 0.60$	5/13
		$p$	$0.281 \pm 0.007$	$0.332 \pm 0.003$	—	$0.02 \pm 0.05$	—	$2.52 \pm 0.15$	4/19
		$\pi^-$	$0.179 \pm 0.008$	$0.191 \pm 0.009$	$0.266 \pm 0.003$	$0.60 \pm 0.02$	$0.15 \pm 0.01$	$45.00 \pm 4.70$	44/25
		$K^-$	$0.235 \pm 0.005$	$0.297 \pm 0.002$	—	$0.80 \pm 0.01$	—	$7.20 \pm 0.53$	3/13
		$\bar{p}$	$0.309 \pm 0.006$	$0.318 \pm 0.007$	—	$0.45 \pm 0.06$	—	$2.12 \pm 0.17$	8/19
	60–92%	$\pi^+$	$0.102 \pm 0.008$	$0.112 \pm 0.006$	$0.292 \pm 0.006$	$0.20 \pm 0.03$	$0.39 \pm 0.03$	$1.82 \pm 0.20$	15/25
		$K^+$	$0.132 \pm 0.008$	$0.272 \pm 0.006$	—	$0.35 \pm 0.04$	—	$0.18 \pm 0.02$	1/13
		$p$	$0.190 \pm 0.008$	$0.209 \pm 0.008$	$0.325 \pm 0.005$	$0.20 \pm 0.03$	$0.21 \pm 0.03$	$0.069 \pm 0.004$	5/19
		$\pi^-$	$0.102 \pm 0.007$	$0.122 \pm 0.008$	$0.302 \pm 0.006$	$0.16 \pm 0.03$	$0.40 \pm 0.07$	$1.74 \pm 0.16$	13/25
		$K^-$	$0.188 \pm 0.008$	$0.241 \pm 0.006$	—	$0.46 \pm 0.08$	—	$0.18 \pm 0.02$	2/13
		$\bar{p}$	$0.204 \pm 0.007$	$0.305 \pm 0.004$	$0.373 \pm 0.007$	$0.45 \pm 0.02$	$0.49 \pm 0.02$	$0.061 \pm 0.007$	7/19
Fig. 2 d-Au 200 GeV	0–20%	$\pi^+$	$0.155 \pm 0.009$	$0.247 \pm 0.005$	$0.468 \pm 0.005$	$0.58 \pm 0.04$	$0.24 \pm 0.03$	$0.97 \pm 0.06$	10/21
		$K^+$	$0.220 \pm 0.012$	$0.230 \pm 0.008$	$0.415 \pm 0.006$	$0.45 \pm 0.03$	$0.28 \pm 0.04$	$0.13 \pm 0.01$	33/18
		$p$	$0.300 \pm 0.006$	$0.310 \pm 0.008$	$0.410 \pm 0.005$	$0.51 \pm 0.04$	$0.25 \pm 0.03$	$0.053 \pm 0.003$	6/21
		$\pi^-$	$0.180 \pm 0.007$	$0.205 \pm 0.008$	$0.434 \pm 0.005$	$0.75 \pm 0.02$	$0.20 \pm 0.02$	$0.99 \pm 0.10$	3/21
		$K^-$	$0.184 \pm 0.009$	$0.211 \pm 0.010$	$0.409 \pm 0.005$	$0.50 \pm 0.02$	$0.28 \pm 0.03$	$0.13 \pm 0.01$	1/18
		$\bar{p}$	$0.281 \pm 0.006$	$0.298 \pm 0.008$	$0.368 \pm 0.005$	$0.64 \pm 0.04$	$0.11 \pm 0.01$	$0.050 \pm 0.003$	16/21
	60–88%	$\pi^+$	$0.150 \pm 0.007$	$0.313 \pm 0.005$	—	$0.84 \pm 0.02$	—	$0.21 \pm 0.02$	23/21
		$K^+$	$0.150 \pm 0.008$	$0.290 \pm 0.008$	$0.384 \pm 0.003$	$0.75 \pm 0.01$	$0.10 \pm 0.01$	$0.036 \pm 0.002$	13/18
		$p$	$0.170 \pm 0.008$	$0.260 \pm 0.006$	$0.405 \pm 0.005$	$0.30 \pm 0.02$	$0.50 \pm 0.02$	$0.015 \pm 0.001$	11/21
		$\pi^-$	$0.155 \pm 0.007$	$0.313 \pm 0.003$	—	$0.84 \pm 0.02$	—	$0.21 \pm 0.02$	17/21
		$K^-$	$0.123 \pm 0.007$	$0.205 \pm 0.005$	$0.428 \pm 0.006$	$0.57 \pm 0.02$	$0.27 \pm 0.02$	$0.035 \pm 0.002$	2/18
		$\bar{p}$	$0.188 \pm 0.008$	$0.293 \pm 0.012$	$0.295 \pm 0.004$	$0.40 \pm 0.03$	$0.25 \pm 0.02$	$0.011 \pm 0.001$	15/21
Fig. 3 Pb-Pb 2.76 TeV	0–5%	$\pi^+ + \pi^-$	$0.132 \pm 0.004$	$0.284 \pm 0.004$	$0.320 \pm 0.005$	$0.62 \pm 0.03$	$0.20 \pm 0.01$	$240.00 \pm 14.00$	5/38
		$K^+ + K^-$	$0.220 \pm 0.009$	$0.321 \pm 0.006$	—	$0.28 \pm 0.06$	—	$36.00 \pm 1.50$	1/33
		$p + \bar{p}$	$0.431 \pm 0.007$	$0.454 \pm 0.014$	—	$0.85 \pm 0.15$	—	$9.70 \pm 0.30$	8/34
	70–80%	$\pi^+ + \pi^-$	$0.127 \pm 0.007$	$0.136 \pm 0.005$	$0.324 \pm 0.004$	$0.38 \pm 0.02$	$0.40 \pm 0.03$	$5.60 \pm 0.27$	5/38
		$K^+ + K^-$	$0.130 \pm 0.010$	$0.267 \pm 0.009$	$0.298 \pm 0.004$	$0.17 \pm 0.04$	$0.15 \pm 0.05$	$0.82 \pm 0.04$	3/33
		$p + \bar{p}$	$0.309 \pm 0.012$	$0.365 \pm 0.013$	$0.380 \pm 0.004$	$0.10 \pm 0.04$	$0.20 \pm 0.05$	$0.30 \pm 0.02$	8/34
Fig. 4 p-Pb 5.02 TeV	0–5%	$\pi^+ + \pi^-$	$0.110 \pm 0.007$	$0.351 \pm 0.012$	$0.392 \pm 0.004$	$0.73 \pm 0.01$	$0.25 \pm 0.06$	$6.37 \pm 0.37$	20/38
		$K^+ + K^-$	$0.162 \pm 0.012$	$0.390 \pm 0.004$	—	$0.49 \pm 0.03$	—	$0.95 \pm 0.04$	3/28
		$p + \bar{p}$	$0.325 \pm 0.016$	$0.361 \pm 0.018$	$0.470 \pm 0.007$	$0.32 \pm 0.02$	$0.42 \pm 0.08$	$0.36 \pm 0.01$	10/36
	60–80%	$\pi^+ + \pi^-$	$0.120 \pm 0.008$	$0.133 \pm 0.009$	$0.342 \pm 0.006$	$0.60 \pm 0.02$	$0.22 \pm 0.02$	$1.65 \pm 0.11$	86/38
		$K^+ + K^-$	$0.158 \pm 0.009$	$0.264 \pm 0.012$	$0.341 \pm 0.004$	$0.30 \pm 0.03$	$0.40 \pm 0.04$	$0.18 \pm 0.01$	28/28
		$p + \bar{p}$	$0.218 \pm 0.004$	$0.422 \pm 0.005$	$0.475 \pm 0.006$	$0.60 \pm 0.02$	$0.22 \pm 0.02$	$0.19 \pm 0.01$	23/36

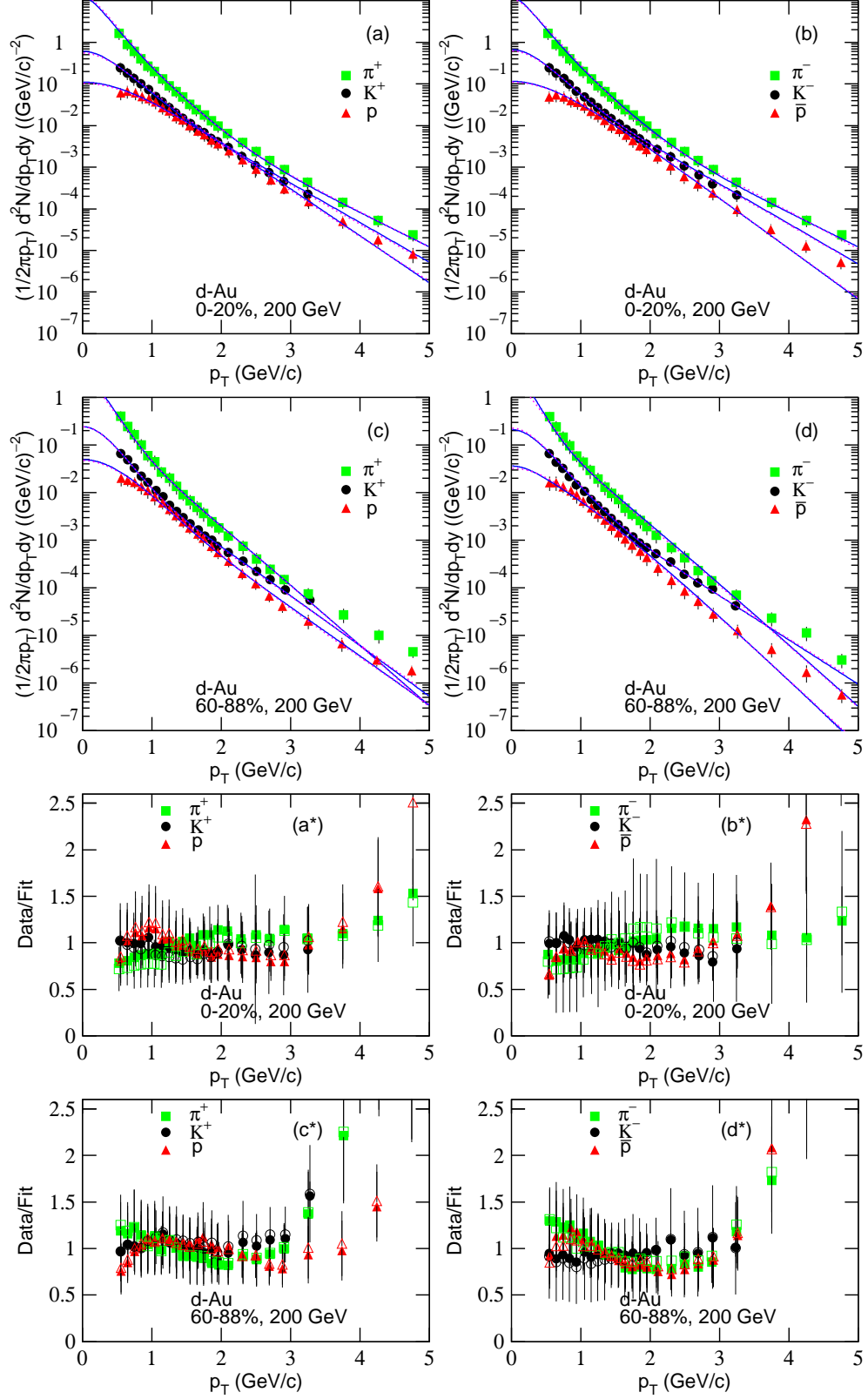


Fig. 2. Same as Fig. 1, but showing the spectra in (a)-(b) 0–20% and (c)-(d) 60–88%  $d$ -Au collisions at  $\sqrt{s_{NN}} = 200$  GeV. The symbols represent the experimental data measured by the PHENIX Collaboration in  $|\eta| < 0.35$  [21].



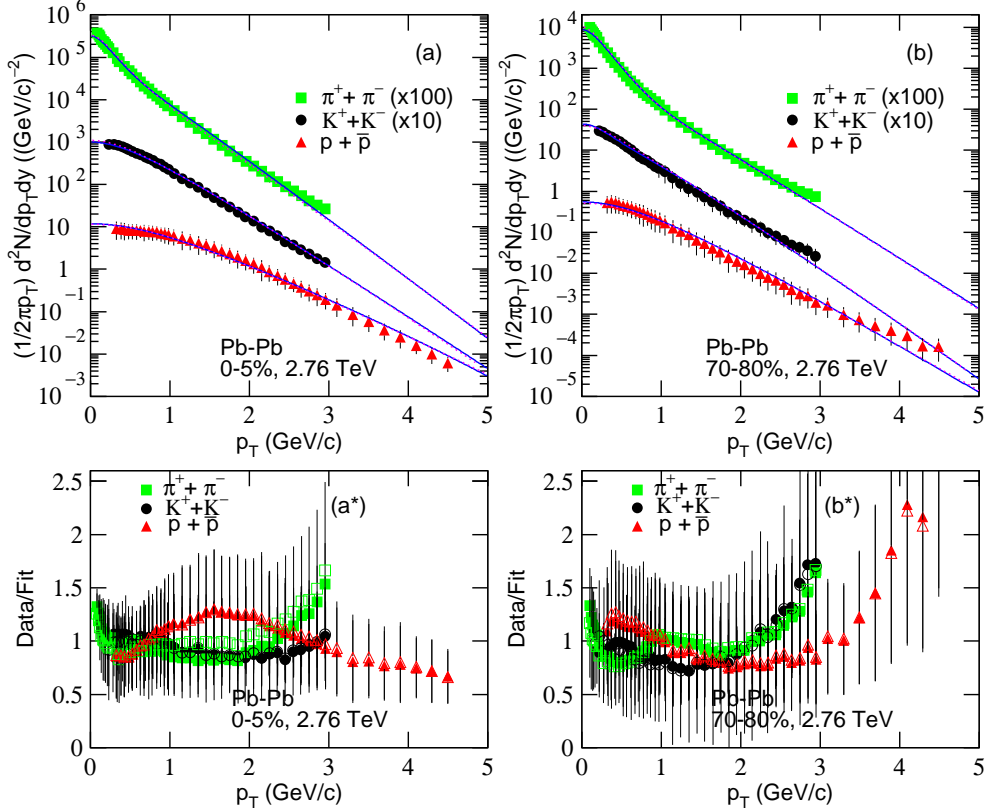


Fig. 3. Transverse momentum spectra of (a)-(b)  $\pi^+ + \pi^-$ ,  $K^+ + K^-$ , and  $p + \bar{p}$  produced in (a) 0–5% and (b) 70–80% Pb-Pb collisions at  $\sqrt{s_{NN}} = 2.76$  GeV, where the spectra for different particles are multiplied by different amounts shown in the panels for the clarity. The symbols represent the experimental data measured by the ALICE Collaboration in  $|y| < 0.5$  [22, 23]. The solid and dotted curves are our results fitted by Eqs. (4) and (8) respectively. The ratios of data/fit corresponding to panels (a) and (b) are presented by panels (a\*) and (b\*) respectively, where the closed and open symbols are the results due to Eqs. (4) and (8) respectively.

show the dependences of  $\langle p_T \rangle_1$  and  $\langle p_T \rangle_2$  on  $C$  respectively. The symbols represent  $\langle p_T \rangle_1$  and  $\langle p_T \rangle_2$  obtained from the fitting functions (Eqs. (4) and (8)) and their parameter values (Tables 1 and 2) over a  $p_T$  range from 0 to 5 GeV/c. The results obtained from the spectra of positive and negative particles are not distinguished to avoid trivialness. One can see that the mean  $p_T$  for particles with large mass, in central collisions, at LHC energy, and in Au-Au (Pb-Pb) collisions are larger than or equal to those for particles with small mass, in peripheral collisions, at RHIC energy, and in  $d$ -Au ( $p$ -Pb) collisions, respectively. These results are in agreement with the trends of effective and kinetic freeze-out temperatures in different centralities, at different energies, and for different system sizes. These results are also in agreement with the trend of effective temperature for emissions of particles with different masses.

Figure 8 is the same as Fig. 7, but it shows the de-

pendences of initial temperature (a)(c)  $T_{i1}$  and (b)(d)  $T_{i2}$  on (a)(b)  $m_0$  and (c)(d)  $C$ , where  $T_{i1}$  ( $T_{i2}$ ) is obtained by the root-mean-square  $p_T$  divided by  $\sqrt{2}$ , i.e.  $\sqrt{\langle p_T^2 \rangle_1/2}$  ( $\sqrt{\langle p_T^2 \rangle_2/2}$ ) according to [37, 38, 39]. The symbols represent the results obtained from the fitting functions (Eqs. (4) and (8)) and their parameter values (Tables 1 and 2) over a  $p_T$  range from 0 to 5 GeV/c. One can see that the trends of  $T_{i1}$  ( $T_{i2}$ ) on particle mass, event centrality, collision energy, and system size are similar to those of  $\langle p_T \rangle_1$  ( $\langle p_T \rangle_2$ ), though  $T_{i1}$  ( $T_{i2}$ ) is smaller than  $\langle p_T \rangle_1$  ( $\langle p_T \rangle_2$ ).

In the rectangular coordinate system which regards the collision point as the original  $O$ , one of the beam directions as the  $Oz$  axis, and the reaction plane as the  $xOz$  plane, the root-mean-square  $p_T$  divided by  $\sqrt{2}$ , i.e.  $\sqrt{\langle p_T^2 \rangle}/2$  also equals to the root-mean-square momentum component ( $\sqrt{\langle p_x^2 \rangle}$  or  $\sqrt{\langle p_y^2 \rangle}$ ) in the transverse plane  $xOy$ . In the rest frame of an isotropic emission

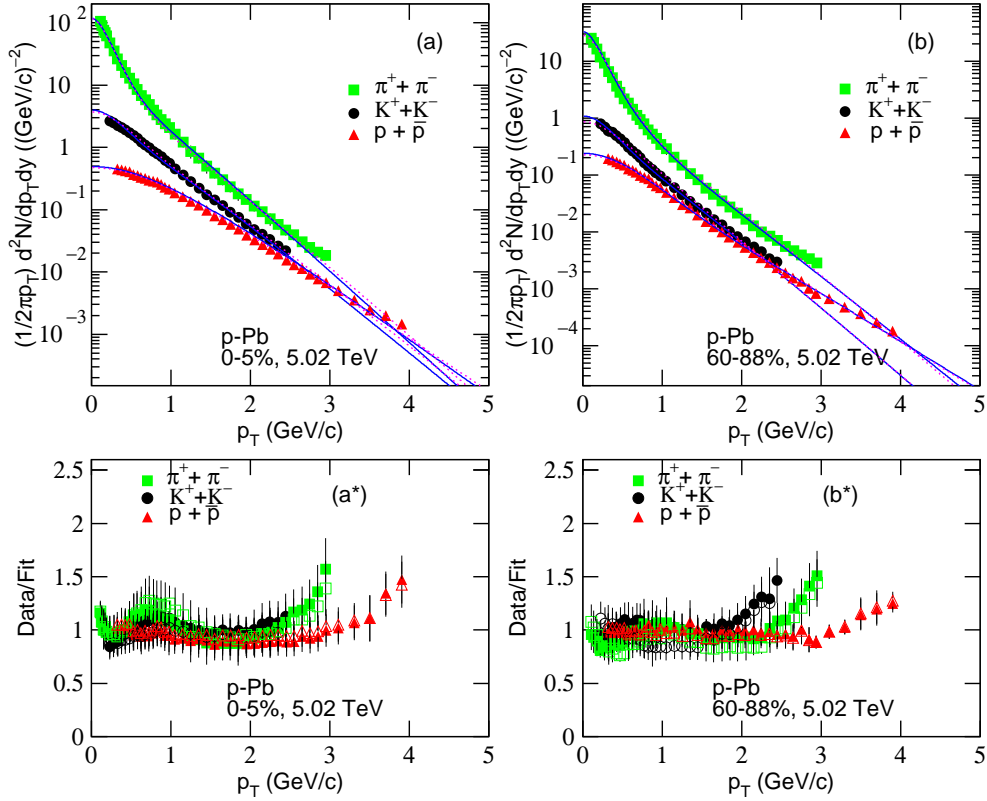


Fig. 4. Same as Fig. 3, but showing the spectra in (a) 0–5% and (b) 60–88%  $p$ -Pb collisions at  $\sqrt{s_{NN}} = 5.02$  GeV. The symbols represent the experimental data measured by the ALICE Collaboration in  $0 < y < 0.5$  [24].

source,  $\sqrt{\langle p_T^2 \rangle}/2$  also equals to  $\sqrt{\langle p_z^2 \rangle}$ . Thus, Fig. 8 also reflects the trends of  $\sqrt{\langle p_x^2 \rangle}$  and  $\sqrt{\langle p_y^2 \rangle}$  in different conditions. In the rest frame of an isotropic emission source, Fig. 8 also reflects the trends of  $\sqrt{\langle p_z^2 \rangle}$  in different conditions.

From Figs. 5–8, one can see that the initial temperature is larger than the effective temperature, and the latter is larger than the kinetic freeze-out temperature. Generally, the chemical freeze-out temperature is between the initial and kinetic freeze-out temperatures, and is approximately equal to the effective temperature. This order is in agreement with the order of time evolution of the interacting system, though both the effective and kinetic freeze-out temperatures are extracted at the kinetic freeze-out. However, we cannot compare directly the four temperatures in most case due to different thermometric scales being used. Like the thermometric scales used in thermal and statistical physics, we need a method to unify different thermometric scales in subatomic physics. To structure the method is beyond the focus of the present work. We shall not discuss this issue in the present work. Or, we may use the quantities

which are model independent to describe the temperatures.

The results presented in Figs. 5–8 also reflect that the violent degree of impact and squeeze in central collisions is comparable with that in peripheral collisions. Meanwhile, the violent degree of impact and squeeze in collisions at LHC energy is comparable with that at RHIC energy. These results are natural due to the fact that the amount of energy deposited in central collisions is comparable with that in peripheral collisions. Meanwhile, the amount of energy deposited in collisions at LHC energy is comparable with that at RHIC energy. The similar results in Au-Au (Pb-Pb) and  $d$ -Au ( $p$ -Pb) collisions confirms the effect of the heaviest nucleus [11] which states that the excitation degree depends on the heaviest nucleus, but not the lightest nucleus and total number of nucleons, in proton(deuteron)-nucleus and nucleus-nucleus collisions at a given  $\sqrt{s_{NN}}$ .

In the above discussions on Figs. 1–8, we have not mentioned the (pseudo)critical temperature at equilibrium, though it is an important baseline in this context. In fact, to obtain experimentally the critical temperature from the fits to data, we have to study the energy

Table 3. Values of intercepts, slopes, and  $\chi^2$  in the linear fittings in Fig. 5, where dof = 1 is not shown in the table to avoid trivialness.

Figure	Collisions	Centrality	Particle	Intercept (GeV)	Slope ( $c^2$ )	$\chi^2$
Fig. 5(a)	Au-Au	Central	positive	$0.294 \pm 0.004$	$0.425 \pm 0.005$	13
			negative	$0.385 \pm 0.003$	$0.294 \pm 0.004$	8
		Peripheral	positive	$0.230 \pm 0.005$	$0.331 \pm 0.005$	47
			negative	$0.232 \pm 0.004$	$0.394 \pm 0.006$	14
	<i>d</i> -Au	Central	positive	$0.371 \pm 0.004$	$0.335 \pm 0.003$	1
			negative	$0.386 \pm 0.004$	$0.243 \pm 0.005$	2
		Peripheral	positive	$0.370 \pm 0.004$	$0.144 \pm 0.003$	1
			negative	$0.345 \pm 0.003$	$0.221 \pm 0.003$	1
	Pb-Pb	Central	positive+negative	$0.361 \pm 0.008$	$0.631 \pm 0.005$	23
		Peripheral	positive+negative	$0.310 \pm 0.005$	$0.449 \pm 0.005$	2
	<i>p</i> -Pb	Central	positive+negative	$0.363 \pm 0.008$	$0.585 \pm 0.003$	1
		Peripheral	positive+negative	$0.317 \pm 0.005$	$0.374 \pm 0.005$	11
Fig. 5(b)	Au-Au	Central	positive	$0.235 \pm 0.002$	$0.110 \pm 0.005$	1
			negative	$0.182 \pm 0.002$	$0.136 \pm 0.003$	1
		Peripheral	positive	$0.168 \pm 0.002$	$0.113 \pm 0.003$	1
			negative	$0.167 \pm 0.003$	$0.092 \pm 0.004$	3
	<i>d</i> -Au	Central	positive	$0.215 \pm 0.003$	$0.124 \pm 0.003$	1
			negative	$0.167 \pm 0.003$	$0.144 \pm 0.004$	1
		Peripheral	positive	$0.161 \pm 0.003$	$0.106 \pm 0.002$	2
			negative	$0.166 \pm 0.003$	$0.092 \pm 0.003$	3
	Pb-Pb	Central	positive+negative	$0.158 \pm 0.003$	$0.291 \pm 0.004$	1
		Peripheral	positive+negative	$0.136 \pm 0.002$	$0.252 \pm 0.005$	1
	<i>p</i> -Pb	Central	positive+negative	$0.140 \pm 0.002$	$0.261 \pm 0.004$	1
		Peripheral	positive+negative	$0.135 \pm 0.004$	$0.185 \pm 0.004$	3

dependent parameters, though the critical temperature can be calculated from first principles such as lattice QCD [40]. Based on an experimental point of view, it is known that there is few related studies on the initial and effective temperatures in literature. In principle, the critical temperature at chemical (kinetic) freeze-out can be obtained from experimental excitation function of chemical (kinetic) freeze-out temperature. However, there is no critical energy being determined in experiments at present. This renders that the critical temperature at chemical (kinetic) freeze-out is not determined in experiments.

Theoretically, the critical temperature at chemical freeze-out is model dependent in some cases, though it is usually less than 170 MeV [41]. For examples, the thermal and statistical model proposes the limiting or approximate critical temperature being about 160 MeV [2, 3, 4, 5, 41]. The calculation based on hydrodynamic evolution proposes the critical temper-

ature being 155 MeV [42]. The theory based on lattice QCD shows the critical temperature being around 160 MeV [43, 44, 45, 46, 47, 48], or as low as 140 MeV [49, 50], which comes from first principles and should be model independent. The analysis based on finite size scaling and hydrodynamics shows the critical temperature is about 165 MeV [51, 52]. The result based on a realistic Polyakov–Nambu–Jona-Lasinio (rPNJL) model gives the critical temperature is 93 MeV [53]. Comparing with the indeterminacy of critical temperature at chemical freeze-out, the study of critical temperature at kinetic freeze-out is lacking in literature.

In consideration of lattice QCD deriving the critical temperature from first principles [40, 43, 44, 45, 46, 47, 48, 49, 50] which is model independent, other models should regard lattice QCD as a standard to revise their calculations to coordinate with the standard. In fact, some models such as the thermal and statistical model [2, 3, 4, 5, 41], the calculation based on hy-

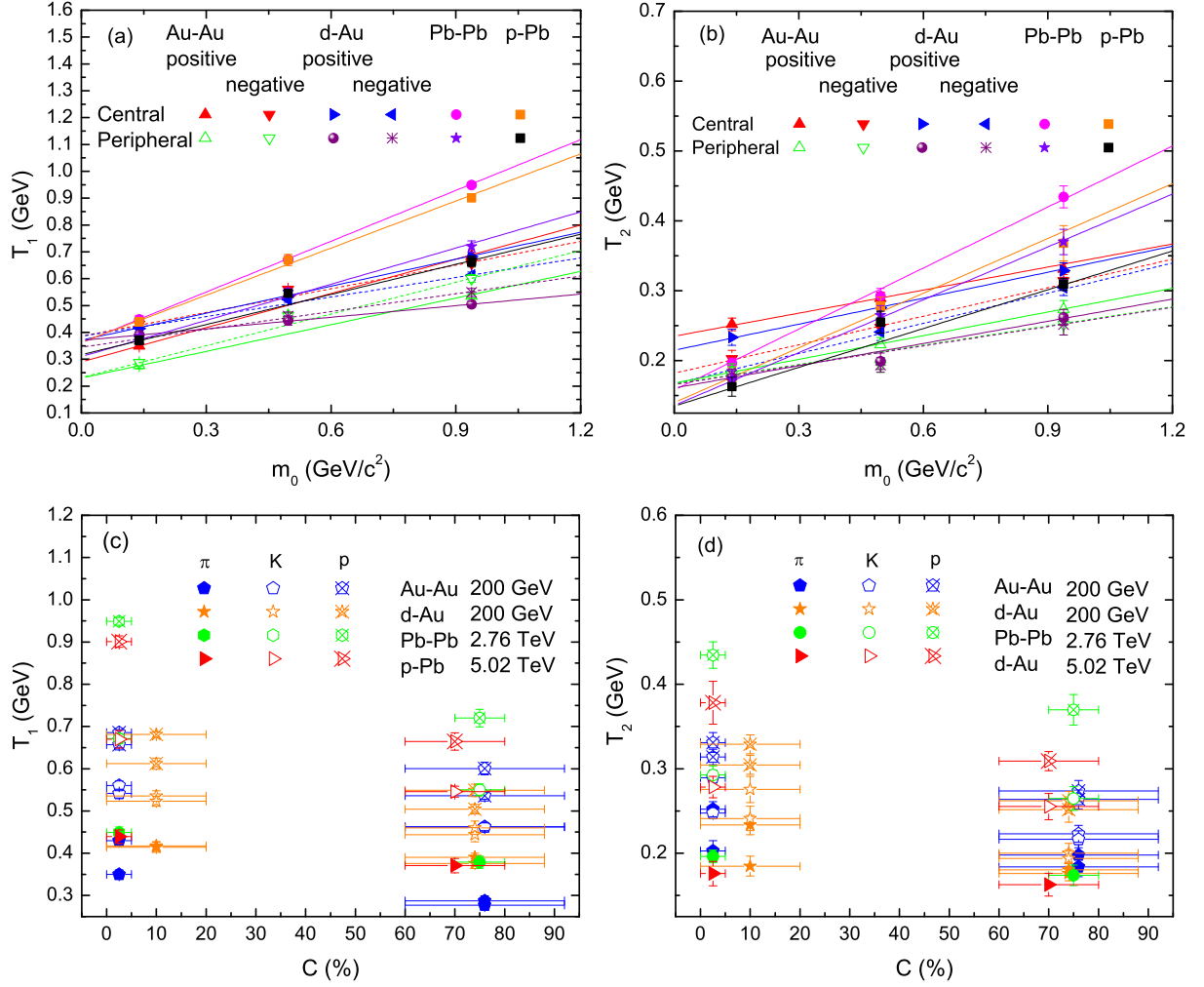


Fig. 5. Upper panel: Dependences of (a)  $T_1$  and (b)  $T_2$  on  $m_0$ . Different symbols represent the results from positive or negative particles produced in central or peripheral Au-Au or  $d$ -Au collisions, or from positive plus negative particles produced in central or peripheral Pb-Pb or  $p$ -Pb collisions. The dashed lines are the fitting results by linear functions for negative particles in Au-Au or  $d$ -Au collisions, and the solid lines are for other cases. Lower panel: Dependences of (c)  $T_1$  and (d)  $T_2$  on  $C$ . The symbols are not distinguished for positive and negative particles in Au-Au and  $d$ -Au collisions, and the positive and negative particles are considered together in Pb-Pb and  $p$ -Pb collisions.

drodynamic evolution [42], and the analysis based on finite size scaling and hydrodynamics [51, 52] are approximately harmonious with lattice QCD with small differences. The rPNJL model [53] studies the critical endpoint which is a different observable which appears at finite baryon density, this is why the critical temperature (93 MeV) there is so low.

From the point of view in physics meaning, the temperatures discussed in Lattice QCD and other related models are transition temperature, which are different from initial, effective, and kinetic freeze-out temperatures discussed in the present work. The three temper-

atures extracted from the multi-component Hagedorn thermal model (standard distribution) are harmonious in relative size. The multi-component Hagedorn thermal model results in larger temperatures than the multi-component standard distribution. The kinetic freeze-out temperature extracted from the multi-component standard distribution is approximately harmonious with the transition temperature discussed in Lattice QCD in order of size.

Based on the thermal and statistical model, the excitation function of chemical freeze-out temperature obtained from particle ratios at mid-rapidity in central

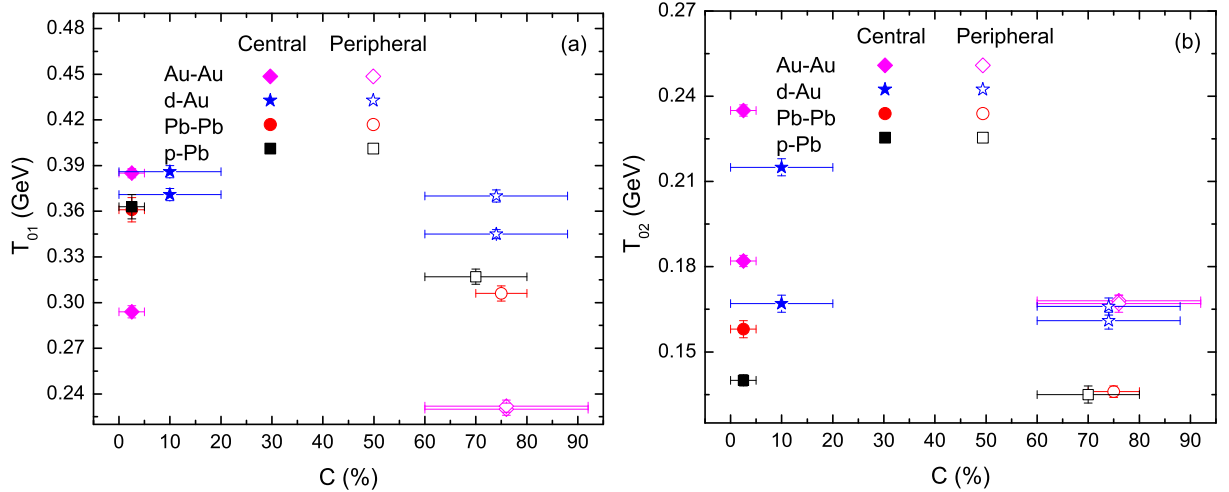


Fig. 6. Dependences of (a)  $T_{01}$  and (b)  $T_{02}$  on  $C$ . Different symbols represent the results from positive or negative particles produced in central or peripheral Au-Au or  $d$ -Au collisions, or from positive plus negative particles produced in central or peripheral Pb-Pb or  $p$ -Pb collisions. The symbols are not distinguished for positive and negative particles in Au-Au and  $d$ -Au collisions, and the positive and negative particles are considered together in Pb-Pb and  $p$ -Pb collisions.

nucleus-nucleus collisions show a quickly increase at a few GeV, a slowly increase at about 10 GeV, and then a saturation at RHIC and LHC energies [2, 3, 4, 5, 41]. The limiting temperature at saturation is  $\sim 164$  MeV [2, 3, 4, 5] or a little less ( $\sim 158$  MeV [41]). Other models [42, 43, 44, 45, 53] are expected to show similar excitation functions of chemical freeze-out temperature with different limiting values, though most excitation functions are lacking in literature. With the limiting or approximate critical temperatures, the limiting baryon chemical potentials are 1 MeV or 0, and the critical baryon chemical potentials obtained from different models [2, 3, 4, 5, 41, 42, 43, 44, 45, 53] are in a wide range from 95 to 720 MeV which are also model dependent in some cases.

In the framework of the blast-wave model or similar model, considering different velocities of transverse flow, the excitation function of kinetic freeze-out temperature obtained from transverse momentum spectra at mid-rapidity in central nucleus-nucleus collisions also show a quickly increase at a few GeV, a slowly change at about 10 GeV, and then a saturation [22, 54] or a slight increase [36, 11] or a continuous decrease [55] or a decrease till the top RHIC energy and then invariability till the LHC energies [56, 57, 58, 59, 60]. The alternative method show a slight increase from the top RHIC energy to the LHC energies [36, 11]. In deeded, the trend of kinetic freeze-out temperature at high en-

ergy is model dependent. As a parameter entangled to kinetic freeze-out temperature, the transverse flow velocity also show a model dependent trend with collision energy.

Before summary and conclusions, we would like to emphasize that the significance of the present work is not solely to describe the  $p_T$  spectra themselves, but mainly to extract various temperatures via the description of the  $p_T$  spectra. Although the hydrodynamic models are excellent, the thermal and statistical models are also useful. In particular, the statistical method is more closer to experiments themselves. We fit the  $p_T$  spectra by taking a sum of two or three statistical distributions after integrating over the necessary rapidity window, in which the contribution of resonance decays at low  $p_T$  is naturally described by the first distribution. Once in a while, an inverse power-law is also added to account for high  $p_T$  part of the data.

The inverse power-law, i.e. the second item in Eqs. (10) and (11), has no contribution to temperatures. To show clearly the trend of the first item in Eqs. (10) and (11), the contribution of the second item therein is not included, which results in the same result from Eqs. (10) and (11) and the fits to be poor at large  $p_T$  in some cases in Figs. 1–4. Although the curvatures in the data are a result of a complex and rich interplay of temperature, flow, and hard scattering process of hadronization as well as decay contributions and even viscosity, the

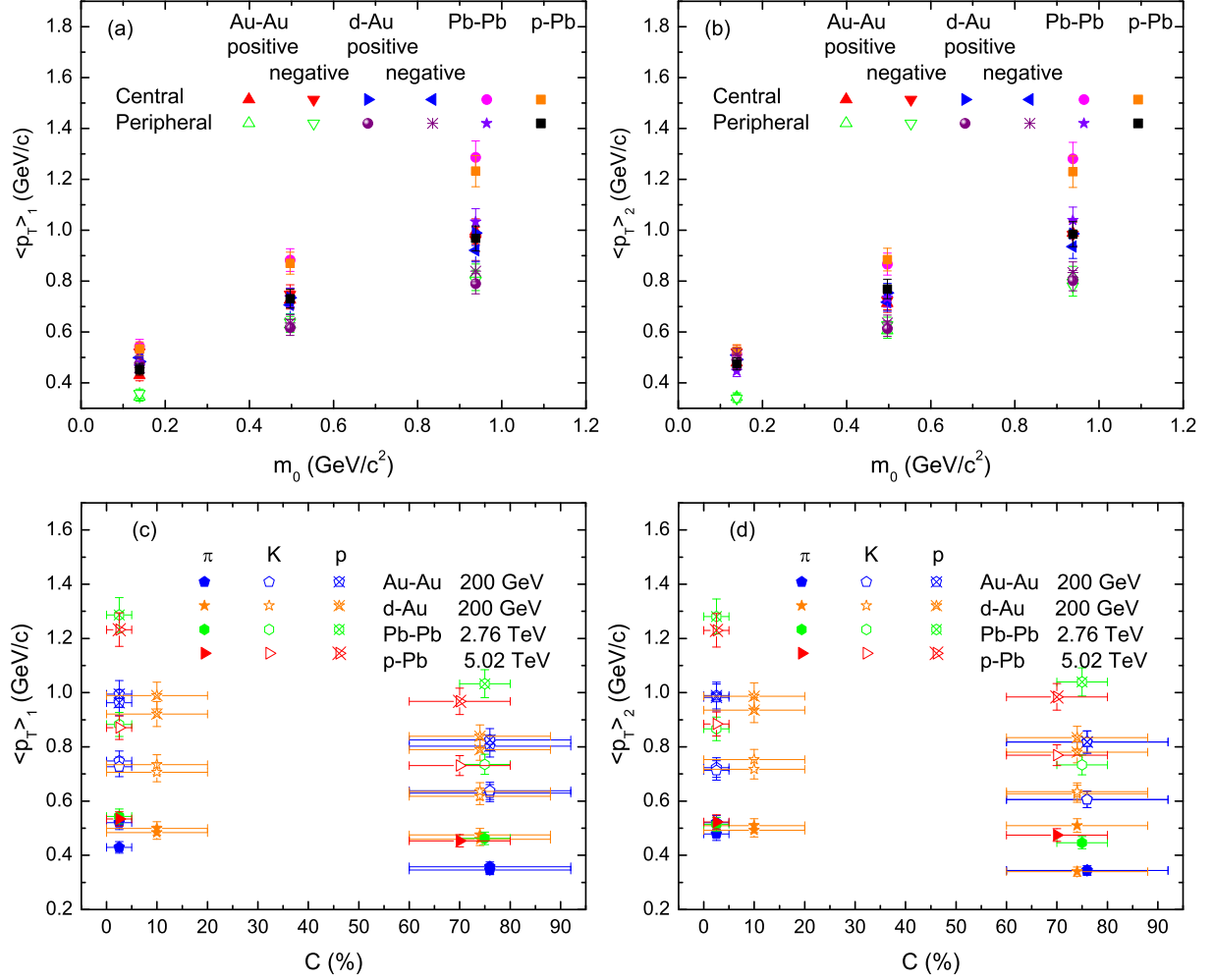


Fig. 7. Upper panel: Dependences of (a)  $\langle p_T \rangle_1$  and (b)  $\langle p_T \rangle_2$  on  $m_0$ . Different symbols represent the results from positive or negative particles produced in central or peripheral Au-Au or  $d$ -Au collisions, or from positive plus negative particles produced in central or peripheral Pb-Pb or  $p$ -Pb collisions. Lower panel: Dependences of (c)  $\langle p_T \rangle_1$  and (d)  $\langle p_T \rangle_2$  on  $C$ . The symbols are not distinguished for positive and negative particles in Au-Au and  $d$ -Au collisions, and the positive and negative particles are considered together in Pb-Pb and  $p$ -Pb collisions.

present work discusses an alternative method to extract various temperatures from the contaminative data as accurately as possible.

The values of effective and kinetic freeze-out temperatures obtained in the present work have only the relative significance due to the fact that the measured functions which can be regarded as “thermometers” or “thermometric scales” used in the present work are different from others such as that of chemical freeze-out temperature which is based on the ratios of different types of particles in thermal and statistical model [2, 3, 4, 5, 41]. In fact, “thermometers” or “thermometric scales” used in subatomic physics should be unified in the framework

of standard distribution which is equal to or closest to the Boltzmann distribution in thermal physics.

In particular, the initial temperature  $T_i$  obtained in the present work is model independent, though it is calculated from the fitted curve. In fact,  $T_i$  can be directly obtained from data themselves if the data points having no large statistical fluctuation. In addition, as a model independent quantity, the half of mean transverse momentum  $\langle p_T \rangle/2$  is expected to represent the sum of contributions of thermal motion and transverse flow, where  $1/2$  is used due to both contributions of projectile and target participants. Let  $k$  denote the fraction in  $\langle p_T \rangle/2$  to contribute to  $T_0$ , we may define  $T_0 \equiv k\langle p_T \rangle/2$  and

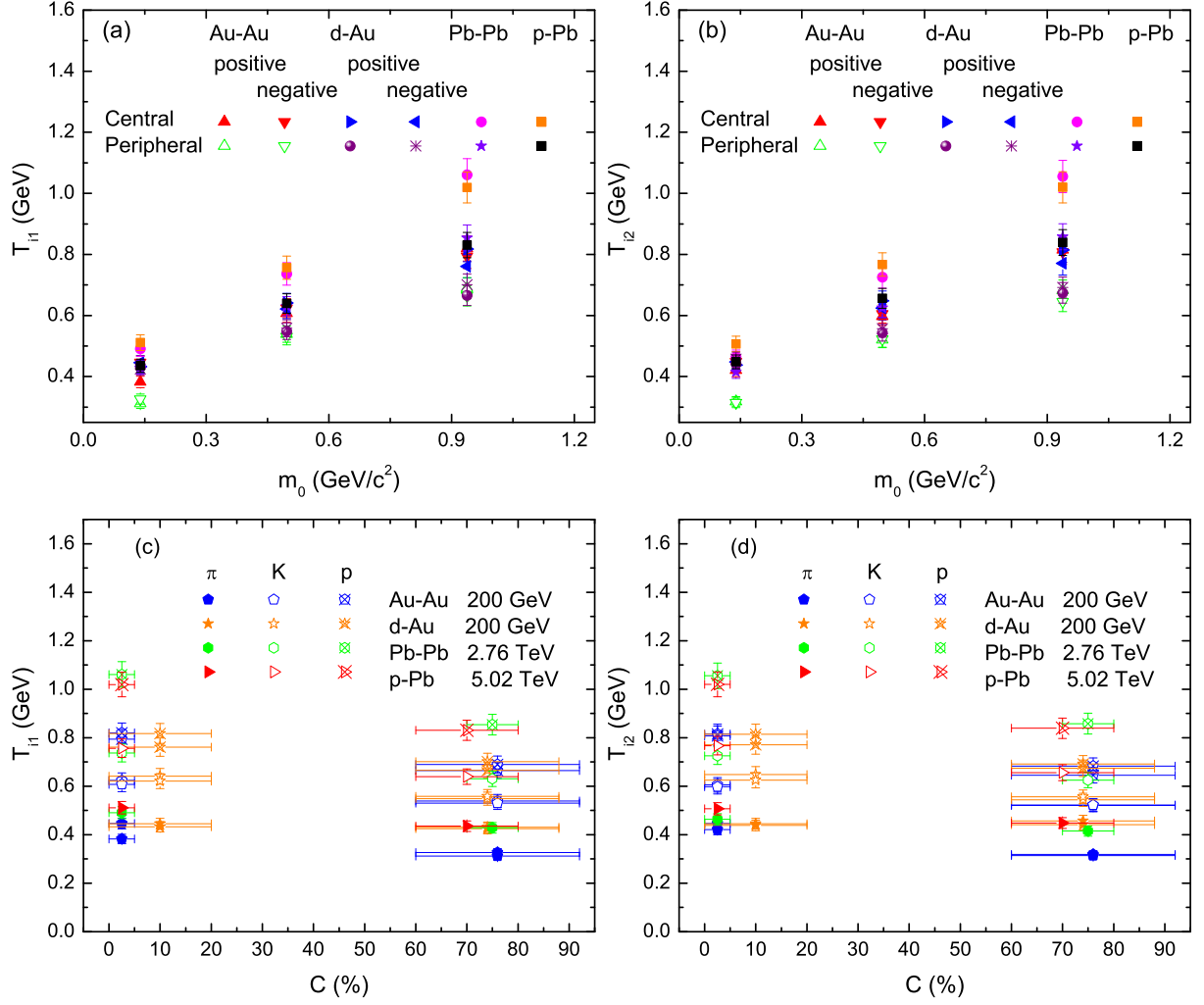


Fig. 8. The same as Fig. 7, but showing the dependences of (a)  $T_{i1}$  and (b)  $T_{i2}$  on  $m_0$ , as well as the dependences of (c)  $T_{i1}$  and (d)  $T_{i2}$  on  $C$ .

$\beta_T \equiv (1 - k)\langle p_T \rangle / 2\overline{m}$ , where  $\overline{m}$  denote the mean energy (mean moving mass) of the considered particles in the source rest frame in which particles are assumed to emit isotropically [36, 11].

The new definition of  $T_0$  ( $\beta_T$ ) is model independent. Contrastively, other definitions or extractions of  $T_0$  ( $\beta_T$ ) are model dependent. In particular, in some cases, the values of  $T_0$  ( $\beta_T$ ) obtained by other methods at high energy are inconsistent due to different given conditions [22, 36, 11, 54, 55, 56, 57, 58, 59, 60]. To obtain consistent results with the alternative method [36, 11], one can revise the given conditions such as the profile function of transverse flow in the blast-wave model [6, 7, 8, 9]. Go a step further, to avoid model dependence, we hope to study  $T_0$  and  $\beta_T$  and their exci-

tation functions from model independent  $\langle p_T \rangle$  in future.

## 4 Summary and conclusions

We summarize here our main observations and conclusions.

(a) The transverse momentum spectra of  $\pi^+$ ,  $\pi^-$ ,  $K^+$ ,  $K^-$ ,  $p$ , and  $\bar{p}$  produced in central and peripheral Au-Au and  $d$ -Au collisions at the top RHIC energy, as well as in central and peripheral Pb-Pb and  $p$ -Pb collisions at LHC energies, have been analyzed by the Hagedorn thermal model and the standard distribution in terms of multi-component. The modelling results are in agreement with the experimental data in low- $p_T$  region measured by the PHENIX Collaboration at the RHIC

and by the ALICE Collaboration at the LHC. The initial, effective, and kinetic freeze-out temperatures are then extracted from the fitting to the transverse momentum spectra.

(b) The initial temperature is larger than the effective temperature, and the latter is larger than the kinetic freeze-out temperature. The chemical freeze-out temperature is between the initial and effective temperatures, and is approximately equal to the effective temperature. This order is in agreement with the order of time evolution of the interacting system, though both the effective and kinetic freeze-out temperatures are extracted at the kinetic freeze-out.

(c) The initial, effective, and kinetic freeze-out temperatures in central collisions are respectively comparable with those in peripheral collisions. The three types of temperatures at LHC energy are respectively comparable with those at RHIC energy. Although the three types of temperatures are different in values, they show similar trends in different centralities and at different energies.

(d) The violent degree of impact and squeeze in central collisions is comparable with that in peripheral collisions, and the violent degree of impact and squeeze in collisions at LHC energy is comparable with that at RHIC energy. These results are caused due to the amount of energy deposited in central collisions being comparable with that in peripheral collisions, and the amount of energy deposited in collisions at LHC energy being comparable with that at RHIC energy.

(e) To use a model independent quantity to represent the kinetic freeze-out temperature  $T_0$  and the transverse flow velocity  $\beta_T$ , we propose to define  $T_0 \equiv k\langle p_T \rangle$  and  $\beta_T \equiv (1 - k)\langle p_T \rangle / \sqrt{m}$ , where  $k$  may be an energy dependent parameter which is needed to study further. Considering  $T_i \equiv \sqrt{\langle p_T^2 \rangle} / 2$  which is also model independent, one has three model independent quantities,  $T_i$ ,  $T_0$ , and  $\beta_T$ . As for the effective temperature, we would like to give it up due to its model dependence and “non-real” one.

### Data Availability

The data used to support the findings of this study are included within the article and are cited at relevant places within the text as references.

### Compliance with Ethical Standards

The authors declare that they are in compliance with ethical standards regarding the content of this paper.

### Conflict of Interest

The authors declare that there are no conflicts of interest regarding the publication of this paper. The funders had no role in the design of the study; in the collection, analysis, or interpretation of the data; in the writing of the manuscript, or in the decision to publish the results.

### Acknowledgments

Communications from Ashfaq Ahmad are highly acknowledged. This work was supported by the National Natural Science Foundation of China under Grant Nos. 11575103 and 11847311, the Chinese Government Scholarship (China Scholarship Council), the Scientific and Technological Innovation Programs of Higher Education Institutions in Shanxi (STIP) under Grant No. 201802017, the Shanxi Provincial Natural Science Foundation under Grant No. 201701D121005, and the Fund for Shanxi “1331 Project” Key Subjects Construction.

### References

- [1] A. Puglisi, A. Sarracino, A. Vulpiani, Phys. Rep. **709**, 1 (2017).
- [2] J. Cleymans, H. Oeschler, K. Redlich, S. Wheaton, Phys. Rev. C **73**, 034905 (2006).
- [3] A. Andronic, P. Braun-Munzinger, J. Stachel, Nucl. Phys. A **772**, 167 (2006).
- [4] A. Andronic, P. Braun-Munzinger, J. Stachel, Acta Phys. Pol. B **40**, 1005 (2009).
- [5] A. Andronic, P. Braun-Munzinger, J. Stachel, Nucl. Phys. A **834**, 237c (2010).
- [6] E. Schnedermann, J. Sollfrank, U. Heinz, Phys. Rev. C **48**, 2462 (1993).
- [7] STAR Collaboration (B.I. Abelev *et al.*), Phys. Rev. C **79**, 034909 (2009).
- [8] STAR Collaboration (B.I. Abelev *et al.*), Phys. Rev. C **81**, 024911 (2010).
- [9] Z.B. Tang, Y.C. Xu, L.J. Ruan, G. van Buren, F.Q. Wang, Z.B. Xu, Phys. Rev. C **79**, 051901(R) (2009).
- [10] H.-R. Wei, F.-H. Liu, R.A. Lacey, J. Phys. G **43**, 125102 (2016).
- [11] H.-L. Lao, F.-H. Liu, B.-C. Li, M.-Y. Duan, R. A. Lacey, Nucl. Sci. Tech. **29**, 164 (2018).
- [12] Z.B. Tang, L. Yi, L.J. Ruan, M. Shao, H.F. Chen, C. Li, B. Mohanty, P. Sorensen, A.H. Tang, Z.B. Xu, Chin. Phys. Lett. **30**, 031201 (2013).
- [13] K. Jiang, Y.Y. Zhu, W.T. Liu, H.F. Chen, C. Li, L.J. Ruan, Z.B. Tang, Z.B. Xu, Phys. Rev. C **91**, 024910 (2015).
- [14] S. Takeuchi, K. Murase, T. Hirano, P. Huovinen, Y. Nara, Phys. Rev. C **92**, 044907 (2015).



- [15] H. Heiselberg, A.M. Levy, Phys. Rev. C **59**, 2716 (1999).
- [16] U.W. Heinz, *Lecture Notes for Lectures Presented at the 2nd CERN-Latin-American School of High-Energy Physics, June 1C14, 2003* (San Miguel Regla, Mexico, 2004). arXiv:hep-ph/0407360 (2004).
- [17] R. Russo, Ph.D. thesis (Universita degli Studi di Torino, Italy, 2015). arXiv:1511.04380 [nucl-ex] (2015).
- [18] J. Cleymans, D. Worku, Eur. Phys. J. A **48**, 160 (2012).
- [19] H. Zheng, L.L. Zhu, Adv. High Energy Phys. **2016**, 9632126 (2016).
- [20] PHENIX Collaboration (A. Adler *et al.*), Phys. Rev. C **69**, 034909 (2004).
- [21] PHENIX Collaboration (A. Adare *et al.*), Phys. Rev. C **88**, 024906 (2013).
- [22] ALICE Collaboration (B. Abelev *et al.*), Phys. Rev. Lett. **109**, 252301 (2012).
- [23] ALICE Collaboration (B. Abelev *et al.*), Phys. Rev. C **88**, 044910 (2013).
- [24] ALICE Collaboration (B. Abelev *et al.*), Phys. Lett. B **728**, 25 (2014).
- [25] R. Hagedorn, Riv. Nuovo Cimento **6**(10), 1 (1983).
- [26] R. Odorico, Phys. Lett. B **118**, 151 (1982).
- [27] UA1 Collaboration (G. Arnison *et al.*), Phys. Lett. B **118**, 167 (1982).
- [28] T. Mizoguchi, M. Biyajima, N. Suzuki, Int. J. Mod. Phys. A **32**, 1750057 (2017).
- [29] ALICE Collaboration (K. Aamodt *et al.*), Phys. Lett. B **693**, 53 (2010).
- [30] A. De Falco for the ALICE Collaboration, J. Phys. G **38**, 124083 (2011).
- [31] ALICE Collaboration (B. Abelev *et al.*), Phys. Lett. B **710**, 557 (2012).
- [32] PHENIX Collaboration (A. Adare *et al.*), Phys. Rev. C **83**, 024909 (2011).
- [33] ALICE Collaboration (B. Abelev *et al.*), Phys. Lett. B **718**, 718 (2012).
- [34] I. Lakomov for the ALICE Collaboration, Nucl. Phys. A **931**, 1179 (2014).
- [35] ALICE Collaboration (B. Abelev *et al.*), Phys. Lett. B **708**, 265 (2012).
- [36] H.-L. Lao, F.-H. Liu, B.-C. Li, M.-Y. Duan, Nucl. Sci. Tech. **29**, 82 (2018).
- [37] L.G. Gutay, A.S. Hirsch, C. Pajares, R.P. Scharenberg, B.K. Srivastava, Int. J. Mod. Phys. E **24**, 1550101 (2015).
- [38] A.S. Hirsch, C. Pajares, R.P. Scharenberg, B.K. Srivastava, arXiv:1803.02301 [hep-ph] (2018).
- [39] P. Sahoo, S. De, S.K. Tiwari, R. Sahoo, Eur. Phys. J. A **54**, 136 (2018).
- [40] M. D’Elia, Nucl. Phys. A **982**, 99 (2019).
- [41] A. Andronic, P. Braun-Munzinger, K. Redlich, J. Stachel, Nature **561**, 321 (2018).
- [42] C. Nonaka, M. Asakawa, Phys. Rev. C **71**, 044904(2005).
- [43] N. Xu (for the STAR Collaboration), Nucl. Phys. A **931**, 1 (2014).
- [44] S. Datta, R.V. Gavai, S. Gupta, Nucl. Phys. A **904–905**, 883c (2013).
- [45] Z. Fodor, S.D. Katz, J. High Energy Phys. **0404**, 050 (2004).
- [46] S. Borsányi, Z. Fodor, C. Hoelbling, S.D. Katz, S. Krieg, C. Ratti, K.K. Szabó, J. High Energy Phys. **1009**, 073 (2010).
- [47] P. Steinbrecher (for the HotQCD collaboration), Nucl. Phys. A **982**, 847 (2019).
- [48] C. Ratti, Rept. Prog. Phys. **81**, 084301 (2018).
- [49] H.-T. Ding, F. Karsch, S. Mukherjee, Int. J. Mod. Phys. E **24**(10), 1530007 (2015).
- [50] H.-T. Ding, P. Hegde, O. Kaczmarek, F. Karsch, A. Lahiri, S.-T. Li, S. Mukherjee, H. Ohno, P. Petreczky, C. Schmidt, P. Steinbrecher, arXiv:1903.04801 [hep-lat].
- [51] R.A. Lacey, Phys. Rev. Lett. **114**, 142301 (2015).
- [52] R.A. Lacey, N.N. Ajitanand, J.M. Alexander, P. Chung, W.G. Holzmann, M. Issah, A. Taranenko, P. Danielewicz, H. Stocker, Phys. Rev. Lett. **98**, 092301 (2007).
- [53] K. Xu, Z.B. Li, M. Huang, EPJ Web Conf. **192**, 00019 (2018).
- [54] A. Andronic, Int. J. Mod. Phys. A **29**, 1430047 (2014).
- [55] S. Das for the STAR collaboration, EPJ Web of Conf. **90**, 08007 (2015).
- [56] S. Zhang, Y.G. Ma, J.H. Chen, C. Zhong, Adv. High Energy Phys. **2015**, 460590 (2015).
- [57] S. Zhang, Y.G. Ma, J.H. Chen, C. Zhong, Adv. High Energy Phys. **2016**, 9414239 (2016).
- [58] STAR Collaboration (L. Adamczyk *et al.*), Phys. Rev. C **96**, 044904 (2017).
- [59] X.F. Luo, Nucl. Phys. A **956**, 75 (2016).
- [60] S. Chatterjee, S. Das, L. Kumar, D. Mishra, B. Mohanty, R. Sahoo, N. Sharma, Adv. High Energy Phys. **2015**, 349013 (2015).